J. Fluid Mech. (1993), *vol.* 248, *pp.* 425–448

Instability of rectangular jets

By CHRISTOPHER K. W. TAM AND ANDREW T. THIES
Department of Mathematics, Florida State University, Tallahassee, FL 32306-3027, USA

(Received 7 April 1992 and in revised form 15 September 1992)

The instability of rectangular jets is investigated using a vortex-sheet model. It is shown that such jets support four linearly independent families of instability waves. Within each family there are infinitely many modes. A way to classify these modes according to the characteristics of their mode shapes or eigenfunctions is proposed. The stability equation for jets of this geometry is non-separable so that the traditional methods of analysis are not applicable. It is demonstrated that the boundary element method can be used to calculate the dispersion relations and eigenfunctions of these instability wave modes. The method is robust and efficient. A parametric study of the instability wave characteristics has been carried out. A sample of the numerical results is reported here. It is found that the first and third modes of each instability wave family are corner modes. The pressure fluctuations associated with these instability waves are localized near the corners of the jet. The second mode, however, is a centre mode with maximum fluctuations concentrated in the central portion of the jet flow. The centre mode has the largest spatial growth rate. It is anticipated that as the instability waves propagate downstream the centre mode would emerge as the dominant instability of the jet.

1. Introduction

Recently there has been a growing interest in the use of non-axisymmetric jets in high-speed propulsive systems. These jets offer possibilities of thrust vectoring, mixing enhancement and noise reduction (see Wlezien & Kibens 1988; Seiner, Ponton & Manning 1986; Krothapalli *et al.* 1989; Gutmark *et al.* 1988; Gutmark, Schadow & Bicker 1990; Schadow *et al.* 1989; Ahuja *et al.* 1990). For high-speed circular jets it is known that the large turbulence structures/instability waves of the jet flow play a key role in the mixing and noise radiation processes (see for example Tam & Burton 1984). It is generally believed that this is also true for non-circular jets. The excited large turbulence structures in mixing layers and jets have been modelled quite successfully using instability wave solutions by Tam & Morris (1985), Gaster, Kit & Wygnanski (1985) and Petersen & Samet (1988). Prior work by Tam & Chen (1979) and Plaschko (1981, 1983) showed that even the broadband spectrum of turbulence in mixing layers and jets can be modelled adequately by the dominant instability wave solutions of the flow.

The stability of elliptic jets has been studied by Crighton (1973) using a vortex-sheet jet model. Morris (1988) re-examined the problem and extended the analysis to jets with more realistic finite-thickness shear layers. An analytic representation of the mean velocity was chosen so that separable solutions of the stability equation in elliptic cylindrical coordinates could be found. In this sense the analysis of the stability of elliptic jets is quite similar to that of the circular jets. For non-axisymmetric jets of other geometry, such as rectangular jets, the stability equation

is non-separable. Thus the traditional methods for finding instability wave solutions are no longer applicable.

Koshigoe and coworkers (Koshigoe & Tubis 1986, 1987; Koshigoe, Gutmark & Schadow 1988) considered the instability of jets of fairly general shape. They proposed a Green's function technique and a generalized shooting method for solving this class of problems. To validate their methods they used them to analyse the stability of elliptic and triangular jets. For elliptic jets, their results were in agreement with those of Morris (1988). More recently Baty & Morris (1989) studied the stability of jets of arbitrary geometry. In their approach they first map the jet cross-section into a standard computational domain. Then a hybrid spectral method is used to solve the eigenvalue problem. They applied their method to incompressible elliptic and rectangular jets and provided some preliminary numerical results. The effectiveness of the method, however, appears to require further testing and study.

The objective of this work is to investigate the instability of rectangular jets. It appears that a systematic study of the instability wave characteristics of these jets has not been done before. Here a vortex-sheet jet model, similar to that used by Crighton (1973) and Morris (1988) in their elliptic jet instability studies, will be employed. Because of the vortex-sheet approximation, the results presented are applicable only to regions of the jet immediately downstream of the nozzle exit where the shear layer is thin. However, most current numerical methods for solving instability of jets of realistic velocity profile require a starting solution to begin the iterative process. The present vortex-sheet model solution could provide a starting value for calculations further downstream.

The instability waves of a rectangular jet can be grouped into four families. Classification of the modes within each family is carried out. The results of a parametric study of the instability wave characteristics is reported in §5 of this paper. Based on these results some general properties of these instability waves are found. It turns out that the first and the third modes of each instability wave family are corner modes. The fluctuations associated with these modes are highly localized near the corners of the jet. The second mode is a centre mode. Its fluctuations are concentrated in the central portion of the jet flow adjacent to the shear layer. Within the range of the present parametric study, the centre mode has the largest spatial growth rate regardless of Mach number and aspect ratio. The possible development of the different instability wave modes in the streamwise direction is discussed at the end of the paper.

To solve the non-separable stability equation, the boundary element method (see, for example, Beskos 1987; Brebbia, Telles & Wrobel 1984) is utilized. In implementing the boundary element method the eigenvalue problem is first recast as a pair of integral equations. These equations are then discretized to form matrix equations which are solved numerically. Numerical convergence of the calculated eigenvalues will be demonstrated. Experience gained in applying this method to circular and rectangular jets indicates that the method is robust and well-suited for solving this class of problems.

2. The eigenvalue problem

Consider a jet of velocity u_j bounded by a vortex sheet B as shown in figure 1. It will be assumed that the cross-section D of the jet is symmetric with respect to the y- and z-axes. The flow is in the x-direction. Jets with cross-sections of this kind include the circular, the elliptic and the rectangular jets. Starting from the linearized

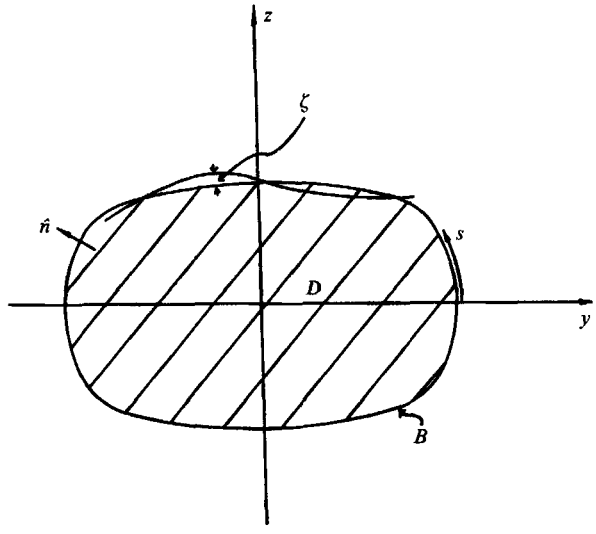

FIGURE 1. Cross-section of a vortex-sheet jet which is symmetric with respect to the y- and z-axes.

continuity, momentum and energy equations of a compressible inviscid fluid it is straightforward to find that the pressures associated with small-amplitude disturbances superimposed on the mean flow inside and outside the jet, p_1 and p_2, are governed by the convective wave equation and the wave equation respectively:

$$\left(\frac{\partial}{\partial t}+u_j\frac{\partial}{\partial x}\right)^2 p_1-a_j^2\nabla^2 p_1=0 \quad \text{inside } D, \tag{2.1}$$

$$\frac{\partial^2 p_2}{\partial t^2}-a_0^2\nabla^2 p_2=0 \quad \text{outside } D, \tag{2.2}$$

where a_0 and a_j are the speeds of sound outside and inside the jet. Let ζ be the displacement of the vortex sheet in the direction $\hat{n}$, normal to the bounding curve B. The dynamic and kinematic boundary conditions at the vortex sheet B are

$$p_1=p_2, \tag{2.3}$$

$$-\frac{1}{\rho_0}\frac{\partial p_2}{\partial n}=\frac{\partial^2\zeta}{\partial t^2}, \tag{2.4}$$

$$-\frac{1}{\rho_j}\frac{\partial p_1}{\partial n}=\left(\frac{\partial}{\partial t}+u_j\frac{\partial}{\partial x}\right)^2\zeta, \tag{2.5}$$

where ρ_0 and ρ_j are the fluid densities outside and inside the jet, respectively. On the left-hand sides of (2.4) and (2.5) the derivatives are in the direction $\hat{n}$.

Instability wave solutions of the above equations and boundary conditions in the form

$$\begin{bmatrix} p_1 \\ p_2 \\ \zeta \end{bmatrix}=\begin{bmatrix} \hat{p}_1(y,z) \\ \hat{p}_2(y,z) \\ \hat{\zeta} \end{bmatrix}e^{i(kx-\omega t)}, \tag{2.6}$$

where ω and k are the angular frequency and axial wavenumber, will now be sought.

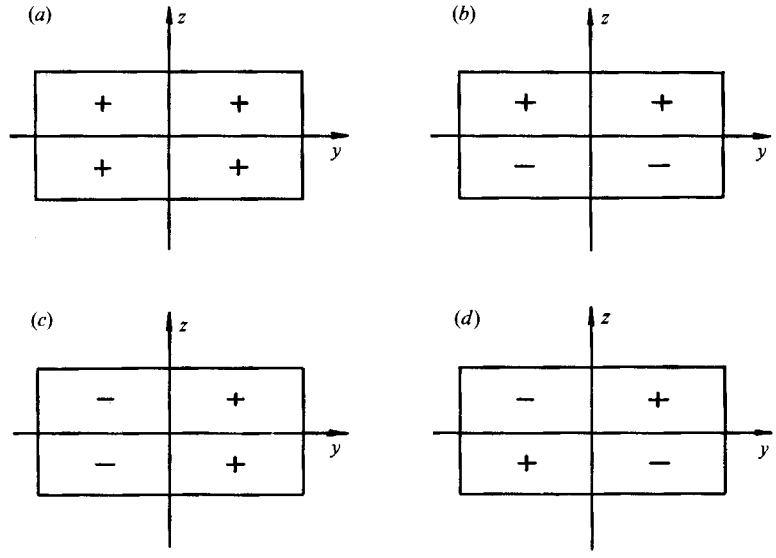

FIGURE 2. The symmetry and antisymmetry of the four families of instabilities of a rectangular jet: (*a*) family 1, (*b*) family 2, (*c*) family 3, (*d*) family 4.

Substitution of (2.6) into (2.1) to (2.5) and eliminating $\hat{\xi}$ leads to the following eigenvalue problem:

$$\nabla_2^2 \hat{p}_1 + \lambda_1^2 \hat{p}_1 = 0 \quad \text{inside } D, \tag{2.7}$$

$$\nabla_2^2 \hat{p}_2 + \lambda_2^2 \hat{p}_2 = 0 \quad \text{outside } D, \tag{2.8}$$

and on the vortex sheet B

$$\hat{p}_1 = \hat{p}_2, \tag{2.9}$$

$$\frac{1}{\rho_j(\omega - u_j k)^2} \frac{\partial \hat{p}_1}{\partial n} = \frac{1}{\rho_0 \omega^2} \frac{\partial \hat{p}_2}{\partial n}, \tag{2.10}$$

where $\lambda_1 = [(\omega - u_j k)^2/a_j^2 - k^2]^{\frac{1}{2}}$ and $\lambda_2 = [\omega^2/a_0^2 - k^2]^{\frac{1}{2}}$. The branch cuts for λ_1 and λ_2 are chosen so that $0 \leqslant \arg \lambda_1, \arg \lambda_2 < \pi$. ∇_2^2 is the two-dimensional Laplacian, i.e.

$$\nabla_2^2 = \left(\frac{\partial^2}{\partial y^2} + \frac{\partial^2}{\partial z^2} \right).$$

Equations (2.7)–(2.10) are homogeneous. In general, the only solution is the trivial solution. However, for a given ω there are special values k, usually complex, for which non-trivial solutions are possible. They are the eigenvalues and the associated eigensolutions. Of special interest are the spatially growing instability waves given by solutions with negative k_i (the imaginary part of k).

Now the y- and z-axes are axes of symmetry of domain D and boundary B. It is easy to verify that the above eigenvalue problem (2.7)–(2.10) is invariant to the following four group transformations:

(*a*) $y \to -y$, $z \to z$, $\hat{p}_i \to \hat{p}_i$, and $y \to y$, $z \to -z$, $\hat{p}_i \to \hat{p}_i$; $i = 1, 2$,

(*b*) $y \to -y$, $z \to z$, $\hat{p}_i \to \hat{p}_i$, and $y \to y$, $z \to -z$, $\hat{p}_i \to -\hat{p}_i$; $i = 1, 2$,

(*c*) $y \to -y$, $z \to z$, $\hat{p}_i \to -\hat{p}_i$, and $y \to y$, $z \to -z$, $\hat{p}_i \to \hat{p}_i$; $i = 1, 2$,

(*d*) $y \to -y$, $z \to z$, $\hat{p}_i \to -\hat{p}_i$, and $y \to y$, $z \to -z$, $\hat{p}_i \to -\hat{p}_i$; $i = 1, 2$.

The symmetry and antisymmetry of the above transformations are illustrated in figure 2. Thus there are four linearly independent families of eigensolutions each satisfying one of the above group transformations.

3. Integral formulation

In this section the differential-equation eigenvalue problem of (2.7) to (2.10) is reformulated into integral equations. This is done by means of the Green's theorem.

3.1. *Boundary integrals*

Let $\boldsymbol{y} = (y, z)$ and $\boldsymbol{y}' = (y', z')$ be coordinate vectors and ∇_2^2 be the two-dimensional Laplacian in the (y, z)-plane. It is well known that the two-dimensional fundamental solution $G_1(\boldsymbol{y}, \boldsymbol{y}')$ satisfying the equation

$$\nabla_2^2 G_1 + \lambda_1^2 G_1 = -\delta(\boldsymbol{y} - \boldsymbol{y}') \tag{3.1}$$

and the boundedness or outgoing wave condition as $|\boldsymbol{y}| \to \infty$ is given by

$$G_1(\boldsymbol{y}, \boldsymbol{y}') = \tfrac{1}{4}\mathrm{i} H_0^{(1)}(\lambda_1 |\boldsymbol{y} - \boldsymbol{y}'|), \tag{3.2}$$

where $H_0^{(1)}(\ )$ is the zeroth-order Hankel function of the first kind.

Let V be the cylindrical volume of unit height generated by translating domain D of figure 1 in the x-direction over a unit distance. By applying Green's theorem, using volume V and functions $\hat{p}_1(\boldsymbol{y})$ of eigenvalue problem (2.7)–(2.10) and $G_1(\boldsymbol{y}, \boldsymbol{y}')$, the integral relation

$$\iiint_V [G_1(\boldsymbol{y}, \boldsymbol{y}') \nabla'^2 \hat{p}_1(\boldsymbol{y}') - \hat{p}_1(\boldsymbol{y}') \nabla'^2 G_1(\boldsymbol{y}, \boldsymbol{y}')] \, \mathrm{d}x' \, \mathrm{d}y' \, \mathrm{d}z'$$

$$= \iint_{B \times 1} \left[G_1 \frac{\partial \hat{p}_1}{\partial n'} - \hat{p}_1 \frac{\partial G_1}{\partial n'} \right] \mathrm{d}A' \tag{3.3}$$

can easily be established. In principle there are two additional terms on the right-hand side of (3.3) involving integrals over the flat surfaces of the cylindrical volume V. However, since the normal derivative terms of the integrand are identically equal to zero on these surfaces, the integrands and the integrals must themselves be zero.

Let s be the arclength of the bounding curve B measured from the positive intersection point on the y-axis as shown in figure 1. The total length of the bounding curve will be taken to be $4\bar{s}$. Note that the integrands of the integrals of (3.3) are independent of x'. Thus by integrating over x' the equation may be simplified to

$$\iint_D [G_1(\boldsymbol{y}, \boldsymbol{y}') \nabla_2'^2 \hat{p}_1(\boldsymbol{y}') - \hat{p}_1(\boldsymbol{y}') \nabla_2'^2 G_1(\boldsymbol{y}, \boldsymbol{y}')] \, \mathrm{d}y' \, \mathrm{d}z'$$

$$= \int_0^{4\bar{s}} \left[G_1(\boldsymbol{y}, s') \frac{\partial \hat{p}_1(s')}{\partial n'} - \hat{p}_1(s') \frac{\partial G_1}{\partial n'}(\boldsymbol{y}, s') \right] \mathrm{d}s'. \tag{3.4}$$

In (3.4) $\hat{p}_1(s')$ and $G_1(\boldsymbol{y}, s')$ are the values of $\hat{p}_1(\boldsymbol{y}')$ and $G_1(\boldsymbol{y}, \boldsymbol{y}')$ on the boundary curve B. Now the two-dimensional Laplacian of $\hat{p}_1$ and G_1 can be eliminated by means of (2.7) and (3.1). It is straightforward to find that upon integrating over the delta function the left-hand side of (3.4) is equal to $\hat{p}_1(\boldsymbol{y})$ if $\boldsymbol{y}$ is an interior point of D, and

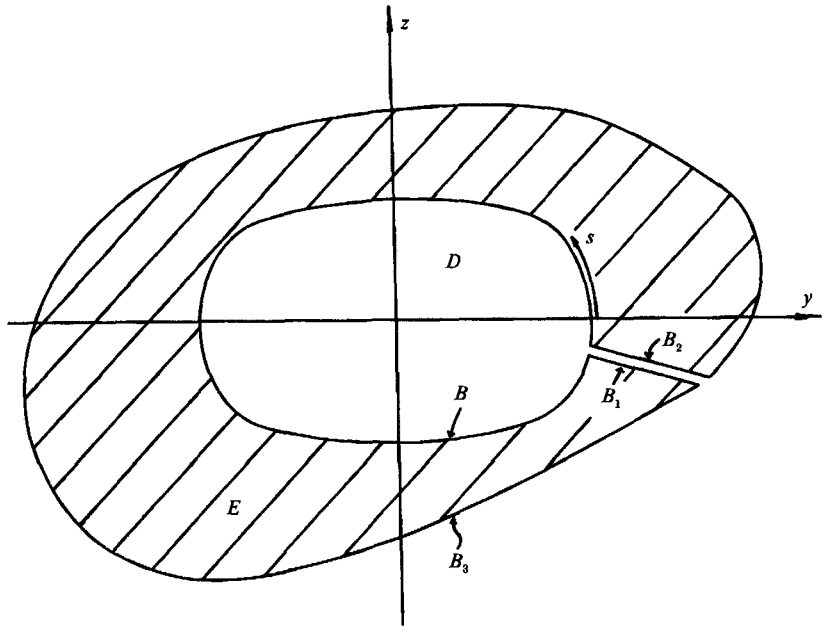

FIGURE 3. Exterior domain E and boundaries.

$\frac{1}{2}\hat{p}_1(s)$ if y is a boundary point with an arclength coordinate s. In this way the boundary integral equation

$$\tfrac{1}{2}\hat{p}_1(s) = \int_0^{4\bar{s}} \left[G_1(s,s') \frac{\partial \hat{p}_1(s')}{\partial n'} - \hat{p}_1(s') \frac{\partial G_1(s,s')}{\partial n'} \right] \mathrm{d}s' \tag{3.5}$$

is derived. Now enclose the domain D of figure 1 by an external curve B_3 with a cut formed by curves B_1 and B_2 as shown in figure 3. In the exterior region E the pressure perturbation is $\hat{p}_2$. Let $G_2(\boldsymbol{y},\boldsymbol{y}')$ be the corresponding fundamental solution satisfying

$$\nabla_2^2 G_2(\boldsymbol{y},\boldsymbol{y}') + \lambda_2^2 G_2(\boldsymbol{y},\boldsymbol{y}') = -\delta(\boldsymbol{y}-\boldsymbol{y}')$$

and the boundedness or outgoing wave condition as $|y| \to \infty$. It is clear that $G_2(\boldsymbol{y},\boldsymbol{y}') = \frac{1}{4}\mathrm{i}H_0^{(1)}(\lambda_2|\boldsymbol{y}-\boldsymbol{y}'|)$. Green's theorem is applied using the functions $\hat{p}_2$ and G_2 and the cylindrical volume of unit height formed by translating the domain E in the x-direction over a unit distance. Upon carrying out steps similar to the above, it is straightforward to obtain, after letting $B_3 \to \infty$ and $B_1 \to B_2$, the following boundary integral equation:

$$\tfrac{1}{2}\hat{p}_2(s) = -\int_0^{4\bar{s}} \left[G_2(s,s') \frac{\partial \hat{p}_2(s')}{\partial n'} - \hat{p}_2(s') \frac{\partial G_2(s,s')}{\partial n'} \right] \mathrm{d}s'. \tag{3.6}$$

Note that the two surface integrals over $B_1 \times 1$ and $B_2 \times 1$ cancel each other because the normal derivative terms of the integrands are exactly opposite in sign. Finally, by means of boundary conditions (2.9) and (2.10), (3.6) may be rewritten as

$$\tfrac{1}{2}\hat{p}_1(s) = -\int_0^{4\bar{s}} \left[\frac{\rho_0 \omega^2}{\rho_j(\omega - u_j k)^2} G_2(s,s') \frac{\partial \hat{p}_1(s')}{\partial n'} - \hat{p}_1(s') \frac{\partial G_2(s,s')}{\partial n'} \right] \mathrm{d}s'. \tag{3.7}$$

Equations (3.5) and (3.7) provide a pair of integral equations for $\hat{p}_1(s)$ and $\partial \hat{p}_1(s)/\partial n$.

3.2. *Integral equations for the four families of instability waves*

It was pointed out in §2 that because of the symmetries of the problem, there are four independent families of eigensolutions. On the boundary B the symmetry and antisymmetry conditions of these solutions can be represented mathematically by the following equations:

$$\hat{p}_1(s) = \sigma_1 \hat{p}_1(2\bar{s}-s) = \sigma_3 \hat{p}_1(2\bar{s}+s) = \sigma_2 \hat{p}_1(4\bar{s}-s), \tag{3.8}$$

where $\sigma_1 = \pm 1$, $\sigma_2 = \pm 1$, $\sigma_3 = \sigma_1 \sigma_2$ and $0 \leqslant s < \bar{s}$. It is easy to see that the four families of eigenfunctions can be obtained by setting the values of σ_1 and σ_2 appropriately; there are four possible combinations of plus and minus one.

The boundary integral equations (3.5) and (3.7) may now be rewritten so as to require integration only over the first quadrant. This is accomplished by using (3.8) and a change of integration variable. The simplified integral equations are

$$\begin{aligned}\tfrac{1}{2}\hat{p}_1(s) = \int_0^{\bar{s}} \Bigg\{ \Bigg[& G_1(s,s') + \sigma_1 G_1(s, 2\bar{s}-s') + \sigma_3 G_1(s, 2\bar{s}+s') \\ & + \sigma_2 G_1(s, 4\bar{s}-s') \Bigg] \frac{\partial \hat{p}_1(s')}{\partial n'} - \Bigg[\frac{\partial G_1}{\partial n'}(s,s') + \sigma_1 \frac{\partial G_1}{\partial n'}(s, 2\bar{s}-s') \\ & + \sigma_3 \frac{\partial G_1}{\partial n'}(s, 2\bar{s}+s') + \sigma_2 \frac{\partial G_1}{\partial n'}(s, 4\bar{s}-s') \Bigg] \hat{p}_1(s') \Bigg\} \mathrm{d}s', \end{aligned} \tag{3.9}$$

$$\begin{aligned}\tfrac{1}{2}\hat{p}_1(s) = -\int_0^{\bar{s}} \Bigg\{ \frac{\rho_0 \omega^2}{\rho_j(\omega - u_j k)^2} \Bigg[& G_2(s,s') + \sigma_1 G_2(s, 2\bar{s}-s') + \sigma_3 G_2(s, 2\bar{s}+s') \\ & + \sigma_2 G_2(s, 4\bar{s}-s') \Bigg] \frac{\partial \hat{p}_1}{\partial n'}(s') - \Bigg[\frac{\partial G_2}{\partial n'}(s,s') + \sigma_1 \frac{\partial G_2}{\partial n'}(s, 2\bar{s}-s') \\ & + \sigma_3 \frac{\partial G_2}{\partial n'}(s, 2\bar{s}+s') + \sigma_2 \frac{\partial G_2}{\partial n'}(s, 4\bar{s}-s') \Bigg] \hat{p}_1(s') \Bigg\} \mathrm{d}s'. \end{aligned} \tag{3.10}$$

For convenience, the notation

$$F \equiv \frac{\rho_j}{\rho_0} \frac{(\omega - u_j k)^2}{\omega^2} \tag{3.11}$$

$$G_i^{(f)}(s,s') \equiv G_i(s,s') + \sigma_1 G_i(s, 2\bar{s}-s') + \sigma_3 G_i(s, 2\bar{s}+s') + \sigma_2 G_i(s, 4\bar{s}-s'); \quad i = 1, 2 \tag{3.12}$$

will be adopted. In the simplified notation, the pair of boundary integral equations of the instability wave problem may be written as

$$\tfrac{1}{2}\hat{p}_1(s) = \int_0^{\bar{s}} \left[G_1^{(f)}(s,s') \frac{\partial \hat{p}_1}{\partial n'}(s') - \frac{\partial G_1^{(f)}}{\partial n'}(s,s') \hat{p}_1(s') \right] \mathrm{d}s', \tag{3.13}$$

$$\tfrac{1}{2} F \hat{p}_1(s) = -\int_0^{\bar{s}} \left[G_2^{(f)}(s,s') \frac{\partial \hat{p}_1}{\partial n'}(s') - F \frac{\partial G_2^{(f)}}{\partial n'}(s,s') \hat{p}_1(s') \right] \mathrm{d}s'. \tag{3.14}$$

4. Discretization by boundary elements

Integral equations (3.13) and (3.14) will be discretized by the method of constant boundary elements (see for example Beskos 1987). The boundary curve B is approximated by $4N$ straightline segments, Γ_i ($i = 1, 2, \ldots, 4N$), over each of which $\hat{p}_1$

and $\partial\hat{p}_1/\partial n$ are taken to be constant. The constant value may be regarded as that at the midpoint of each line segment. The locations of these midpoints are denoted by s_i $(i = 1, 2, \ldots, 4N)$. The equality of the integral equations will be enforced at $s = s_i$ $(i = 1, 2, \ldots, N)$, i.e. in the first quadrant. Upon introducing the notation

$$p_i = \hat{p}_1(s_i), \quad g_i = \frac{\partial \hat{p}_1}{\partial n}(s_i),$$

$$\mu_{ij} = \int_{\Gamma_j} G_1(s_i, s')\,\mathrm{d}s', \quad \nu_{ij} = \int_{\Gamma_j} \frac{\partial G_1}{\partial n'}(s_i, s')\,\mathrm{d}s', \tag{4.1}$$

$$\bar{\mu}_{ij} = \int_{\Gamma_j} G_2(s_i, s')\,\mathrm{d}s', \quad \bar{\nu}_{ij} = \int_{\Gamma_j} \frac{\partial G_2}{\partial n'}(s_i, s')\,\mathrm{d}s',$$

$$\mu_{ij}^{(f)} = \mu_{ij} + \sigma_1 \mu_{i,\,2N-j+1} + \sigma_3 \mu_{i,\,2N+j} + \sigma_2 \mu_{i,\,4N-j+1},$$

and similar notation for $\bar{\mu}_{ij}^{(f)}$, $\nu_{ij}^{(f)}$ and $\bar{\nu}_{ij}^{(f)}$, integral equations (3.13) and (3.14) may be cast into the following matrix form:

$$[\tfrac{1}{2}\delta_{ij} + \nu_{ij}^{(f)}]\boldsymbol{p} - [\mu_{ij}^{(f)}]\boldsymbol{g} = 0, \tag{4.2}$$

$$F[-\tfrac{1}{2}\delta_{ij} + \bar{\nu}_{ij}^{(f)}]\boldsymbol{p} - [\bar{\mu}_{ij}^{(f)}]\boldsymbol{g} = 0. \tag{4.3}$$

The vectors $\boldsymbol{p}$ and $\boldsymbol{g}$ have elements p_i and g_i $(i = 1, 2, \ldots, N)$.

In general, the matrix equations (4.2) and (4.3) have the trivial solution as the only solution. In order for a non-trivial solution to exist, the determinant of the combined coefficient matrix must be equal to zero. This leads to the instability wave dispersion relation

$$D(\omega, k) \equiv |\boldsymbol{M}(\omega, k)| \equiv \begin{vmatrix} [\tfrac{1}{2}\delta_{ij} + \nu_{ij}^{(f)}] & -[\mu_{ij}^{(f)}] \\ F[-\tfrac{1}{2}\delta_{ij} + \bar{\nu}_{ij}^{(f)}] & -[\bar{\mu}_{ij}^{(f)}] \end{vmatrix} = 0. \tag{4.4}$$

For a given angular frequency ω the roots of (4.4), the eigenvalues k, are generally complex. In this work they are determined computationally. Once an eigenvalue k is found, the eigenvector can be calculated by solving (4.2) and (4.3) in a straightforward manner.

5. Numerical results

As soon as the jet fluid leaves the nozzle exit, viscosity and mixing will smooth out the sharp corners of the cross-section of the jet. To take this fact into account the rectangular jets considered here are assumed to have slightly rounded corners. Numerical experiments using different sizes of round-off ellipses (up to $\frac{1}{10}$ of the corresponding side width of the jet) have been carried out. It is found that both the growth rate and wavelength of the instability waves are not sensitive to the size of the corner. For computational purposes the corners are rounded off by ellipses with semi-axes equal to $\frac{1}{20}$ of the corresponding side width of the jet. This is illustrated in figure 4.

To compute the complex wavenumber (eigenvalue) of an instability wave, the first step is to calculate the elements of the determinant in (4.4). In the Appendix it is shown that the integrals involved may be transformed into a form with non-singular

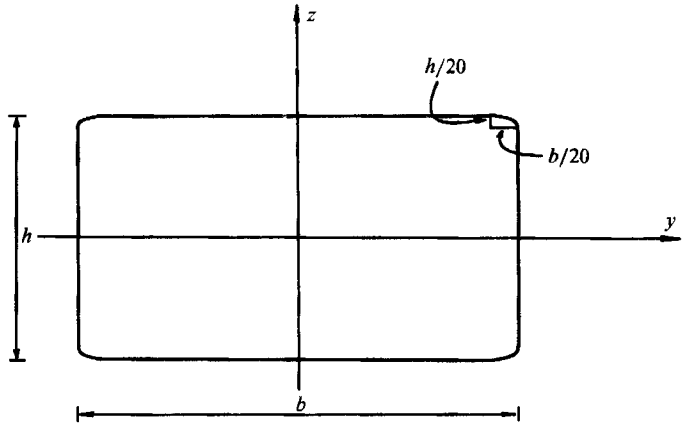

FIGURE 4. Cross-section of rectangular vortex-sheet jets used in computation.

N	Re kR_j	Im kR_j	Absolute error
10	1.0236236247	−0.5451051850	0.0005476318
20	1.0240458358	−0.5451471909	0.0001503520
30	1.0241272918	−0.5451557723	0.0000684562
40	1.0241562628	−0.5451589787	0.0000393175
50	1.0241698365	−0.5451605732	0.0000256578
60	1.0241772879	−0.5451615024	0.0000181546
70	1.0241818118	−0.5451620909	0.0000135979
80	1.0241847870	−0.5451625088	0.0000105975
Exact	1.0241951770	−0.5451645956	—

TABLE 1. Circular jet, family 1, mode 1, Strouhal number = 0.3, Mach number = 1.5, 5 Gaussian nodes per element

N	Re kR_j	Im kR_j	Absolute error
10	1.0236440325	−0.5451264324	0.0005524642
20	1.0240538330	−0.5451555890	0.0001416307
30	1.0241320365	−0.5451608269	0.0000632529
40	1.0241594806	−0.5451624513	0.0000357607
50	1.0241722615	−0.5451632120	0.0000229572
70	1.0241834603	−0.5451638973	0.0000117375
90	1.0241880801	−0.5451641749	0.0000071094
Exact	1.0241951770	−0.5451645956	—

TABLE 2. Circular jet, family 1, mode 1, Strouhal number = 0.3, Mach number = 1.5, 20 Gaussian nodes per element

integrands. In this work, the integrals are computed by Gaussian quadratures using five or more Gaussian points. Once the computer program for calculating the elements and the value of the determinant in (4.4) is completed, a two-step method is used to determine the eigenvalues. First, an initial search for the roots of (4.4) using the grid-search technique described by Tam & Hu (1989) is carried out. This initial search is necessary in order to provide good starting values for eigenvalue refinement. In performing the grid search the complex kh-plane is divided into smaller

subregions by a rectangular grid. The value of the dispersion function $D(\omega, k)$ is calculated at each grid point. A plotting subroutine is then called to execute a two-dimensional interpolation of this set of values and construct the two families of curves $\mathrm{Re}\,(D) = 0$ and $\mathrm{Im}\,(D) = 0$. The intersections of these curves provide a first estimate of the locations of the zeros of D.

The second step is to refine the eigenvalues. In this study this is done by applying Newton's iteration method. Central to the Newton's iteration method is an algorithm to calculate the derivative $\partial D/\partial k$. Since D is a large-order determinant the most efficient way of computing this derivative is by the Trace theorem of Davidenko (1960). The Trace theorem has been used effectively for instability wave calculations by Bridges & Morris (1984). If $k^{(m)}$ is the mth iterate then Newton's method together with the Trace theorem leads to the recurrence formula

$$k^{(m+1)} = k^{(m)} - \left[\mathrm{Trace}\left(\boldsymbol{M}^{-1}\frac{\partial}{\partial k}\boldsymbol{M}\right)\right]^{-1}_{k=k^{(m)}},$$

where $\boldsymbol{M}$ is the matrix of (4.4). In this investigation the iteration is allowed to continue until the following stopping criteria are met:

(i) $|k^{(m+1)} - k^{(m)}| \leqslant 10^{-4}|k^{(m)}|$,

(ii) $|D^{(m+1)}| \leqslant 10^{-4}|\text{first element of } \boldsymbol{M}^{(m+1)}|\,|\text{cofactor}|$.

5.1. *Circular jets*

To demonstrate the accuracy and suitability of the boundary element method for instability calculation, results of the circular jet instability wave calculated by this method will be compared with the exact solutions. In circular jets the four families of eigensolutions have the following angular dependence:

$$\text{Family 1:}\quad \cos(2n\theta),$$

$$\text{Family 2:}\quad \sin(2n+1)\,\theta,$$

$$\text{Family 3:}\quad \cos(2n+1)\,\theta,$$

$$\text{Family 4:}\quad \sin(2n\theta),$$

where $n = 0, 1, 2, \ldots$.

Table 1 shows the wavenumber of the family 1, mode 1 instability wave of a Mach 1.5 circular jet at Strouhal number (fD_j/u_j) 0.3 calculated by the boundary element method where D_j is the jet diameter. N is the number of boundary elements used. By comparing with the exact eigenvalue it appears that three-figure accuracy is obtained using as few as 10 elements. As expected, the accuracy of the computed results improves as the number of elements used increases. From this table it is clear that there is size convergence as $N \to \infty$ in the computed eigenvalue. In this demonstration five Gaussian points are used in evaluating the integrals of the elements of the determinant. Table 2 shows the same calculation except that the number of Gaussian points is increased to 20. Judging from the results of the two tables it becomes apparent that if three-figure accuracy is required then integration employing five Gaussian points is sufficient.

Figure 5 (*a*, *b*) shows the calculated dispersion relations, kR_j versus $\omega R_j/u_j$, of the first three modes of the family 1 instability waves of a Mach 1.5 jet for dimensionless frequency $\omega R_j/u_j$ up to 3.0 (R_j is the radius of the jet). The real and imaginary parts of the exact wavenumber are also plotted on these figures. In the boundary element

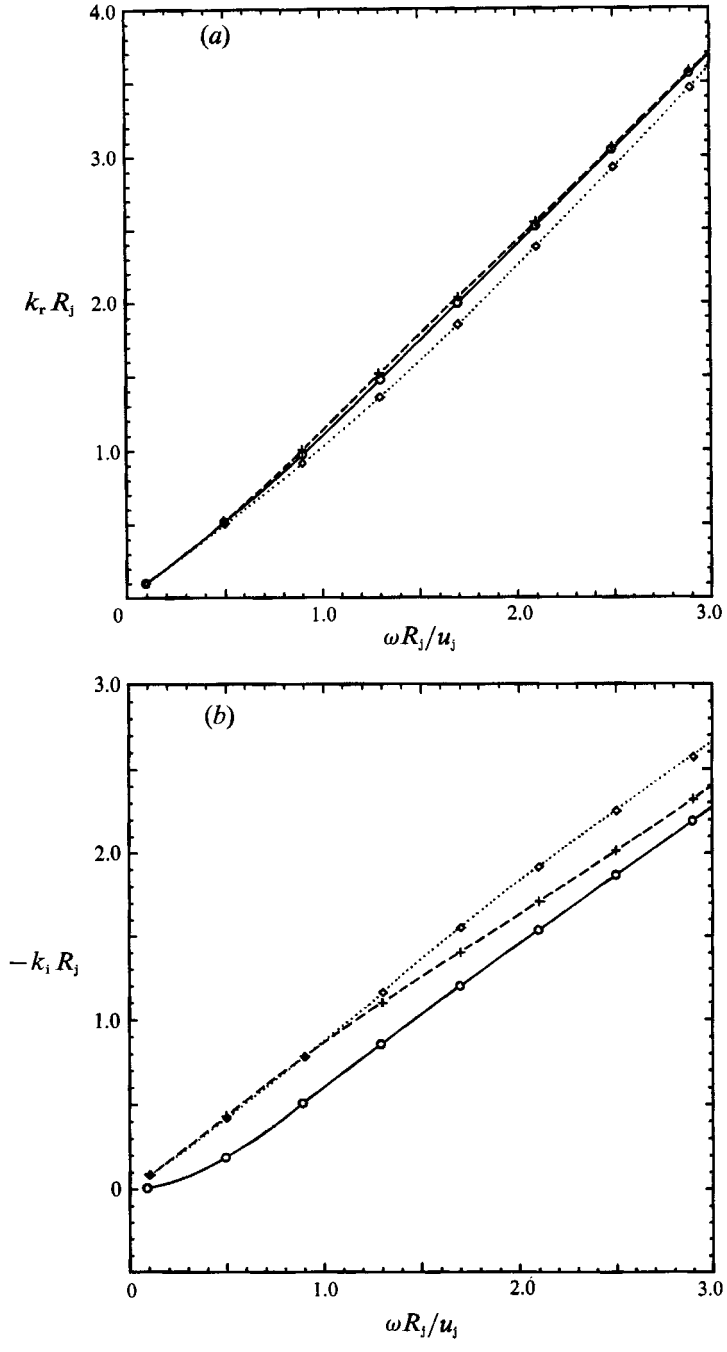

FIGURE 5. Dispersion relation for family 1 of a vortex-sheet, Mach 1.5, circular jet. Exact solution: ○, mode 1; +, mode 2; ◇, mode 3. Boundary element solution: ——, mode 1; – – – –, mode 2; · · · · ·, mode 3. (*a*) $k_r R_j$ versus $\omega R_j/u_j$, (*b*) $-k_i R_j$ versus $\omega R_j/u_j$.

calculation 15 elements are used. Clearly there is good agreement with the exact results over the entire range of frequencies.

Figure 6 gives the spatial distribution of the family 2, mode 2 pressure eigenfunction, $|p|$, in the first quadrant computed by the boundary element method.

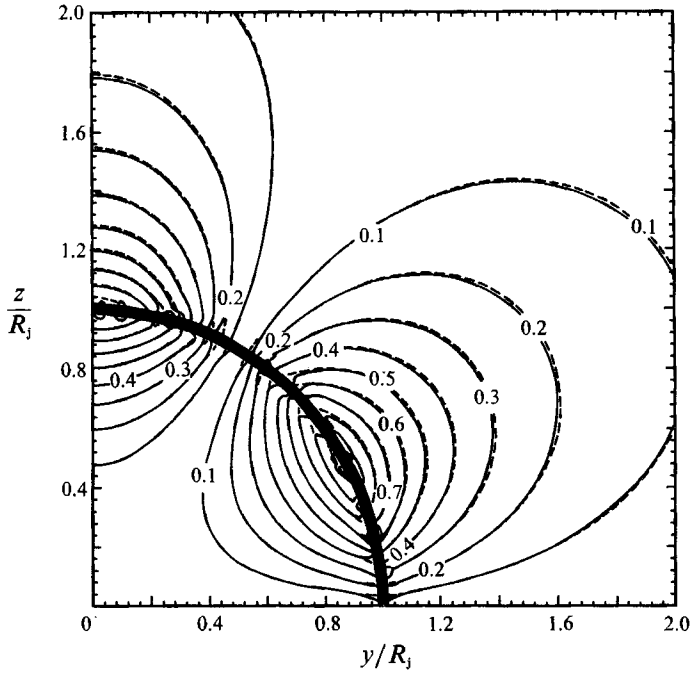

FIGURE 6. Distribution of $|p|$ in the first quadrant of a Mach 1.5, circular jet for family 2, mode 2 ($\sin 3\theta$ dependence) with $\omega R_j/u_j = 0.3\pi$ and $kR_j = 0.9888$–0.8452i: – – – –, exact solution; ——, boundary element solution.

Eight boundary elements are used. Also shown, as dashed lines, is the exact eigenfunction distribution. It is evident that the difference between the two distributions is quite minor. This is true both inside and outside the jet. Based on these and other similar results (not discussed here because of space limitations) it is believed that the boundary element method can be trusted to provide fairly accurate calculations of jet instability wave characteristics even when as few as 10 elements per quadrant are employed.

5.2. *Modal classification for rectangular jets*

Each family of instability waves of a rectangular jet consists of infinitely many modes. Unlike a circular jet there does not seem to be a natural way to classify these wave modes. The modal classification scheme adopted in this study is by no means unique. However, it does have the advantage that the mode numbers assigned, regardless of family, appear to correlate with some of the characteristics of the instability waves. This point will become apparent later.

Consider the special case of a square jet. Extensive computation indicates that the propagation characteristics and eigenfunction distribution of an instability wave mode can change appreciably with Strouhal number, $\omega h/u_j$. However, at low Strouhal number, say $\omega h/u_j = 0.1$, the instability waves of a square jet resemble those of a circular jet. For instance, the first mode of the first family of instability waves of a circular jet has a pressure eigenfunction distribution, $|p|$, uniform over the entire thin shear layer. For the higher-order modes the spatial distribution of $|p|$ oscillates as a function of the arclength s. The mode number is exactly equal to the number of maxima in the first quadrant. It turns out that the eigenfunctions of the square jet also exhibit very similar characteristics. An example is shown in figure 7.

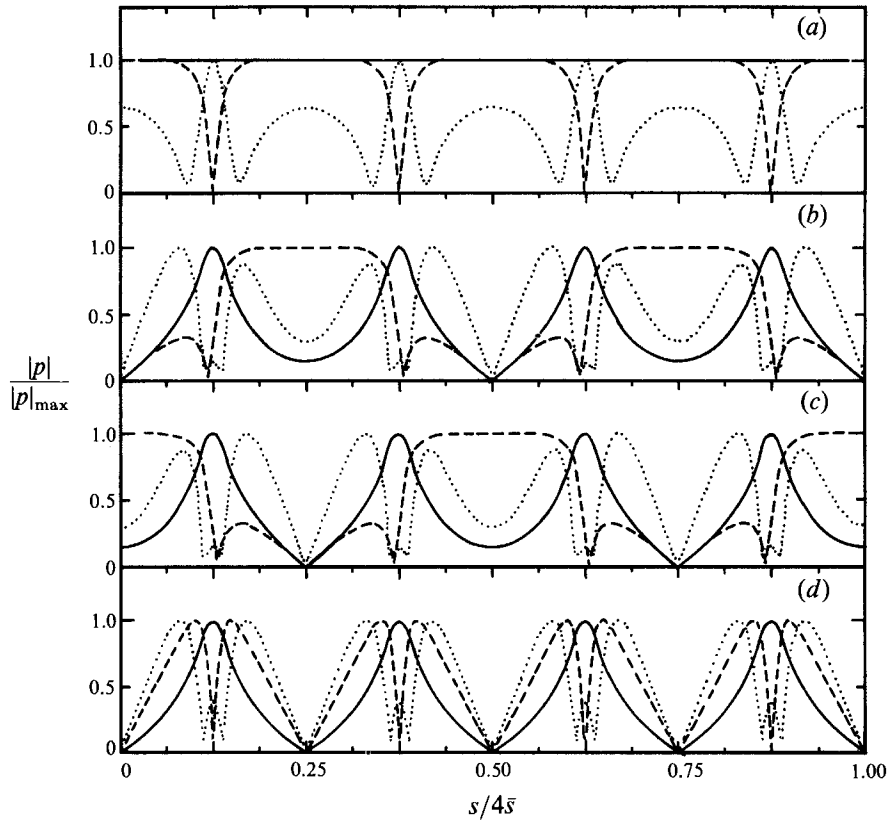

FIGURE 7. Distribution of $|p|$ along the thin shear layer of a Mach 1.5, square jet when $\omega h/u_j = 0.1$: ——, mode 1; – – –, mode 2; · · · · ·, mode 3. (*a*) Family 1, (*b*) family 2, (*c*) family 3, (*d*) family 4.

In this figure the eigenfunctions are for a cold (same total temperature inside and outside the jet), 1.5 Mach number jet, but the Mach number is unimportant. The number of maxima remains the same for other Mach number jets. In the following the mode number of an instability wave of a square jet is decided by the number of maxima of $|p|$ along the shear layer in the first quadrant at $\omega h/u_j = 0.1$. For waves at other Strouhal numbers the mode number is obtained by analytic continuation of this special solution in frequency space. Computationally the continuation is carried out by incremental changes in $\omega h/u_j$. The eigenvalue refinement is done by the Newton's iteration process. Similarly for rectangular jets, the instability waves are obtained by analytic continuation of those of the square jet regarding the aspect ratio as a continuous parameter. The mode number is kept the same in the analytic continuation process. In this way the mode numbers of the instability waves of rectangular jets are established.

5.3. *Dispersion relations, eigenfunctions and some prominent characteristics of the instability waves of rectangular jets*

Extensive computations of the dispersion relations and eigenfunctions of the instability waves of rectangular jets at subsonic and supersonic Mach numbers have been carried out. Here a typical sample of the computed results and the highlights of some of the general characteristics of the instability waves will be reported.

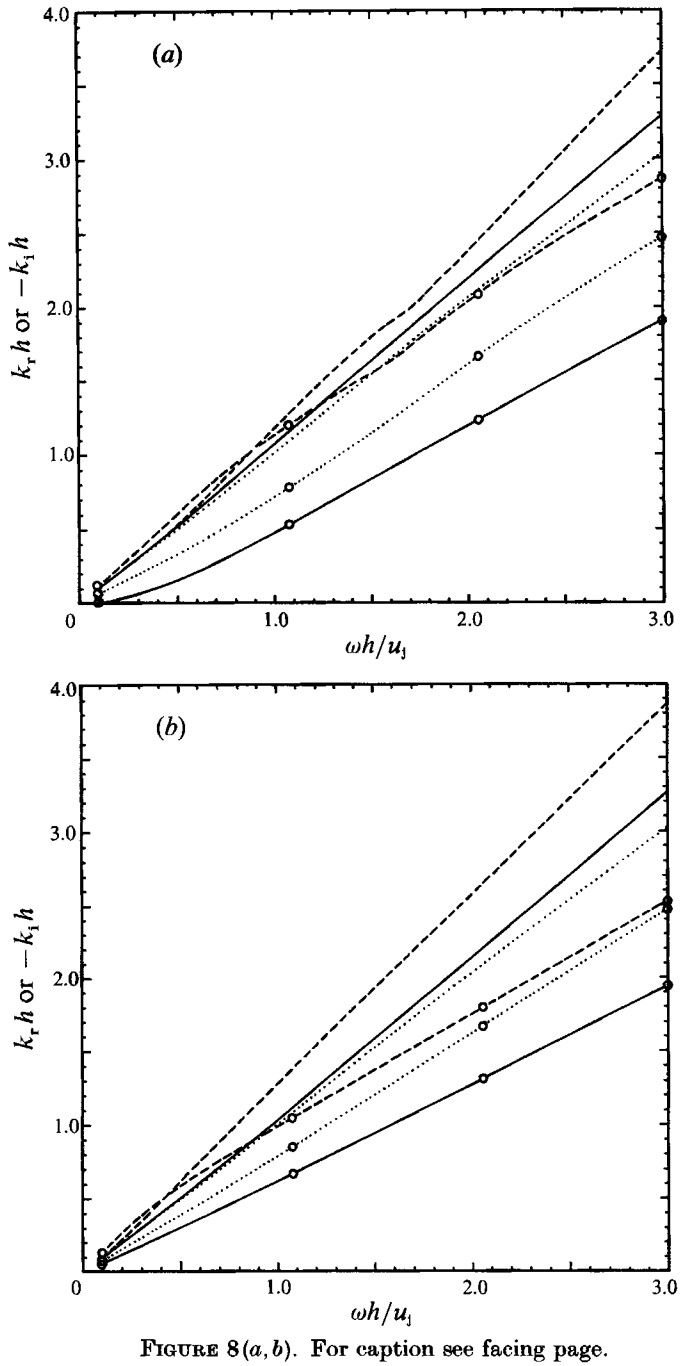

FIGURE 8(a, b). For caption see facing page.

Figure 8(a) shows the dispersion relations for the first three modes of the family 1 instability waves of a cold, Mach 1.5, rectangular jet with aspect ratio 2 (39 boundary elements were used in the calculation). Similar dispersion relations for the other three families are given in figure 8(b–d). These are typical dispersion relations at supersonic Mach numbers. One distinctive feature of these dispersion relations is that the real part of the wavenumber, k_r, is almost a linear function of frequency ω.

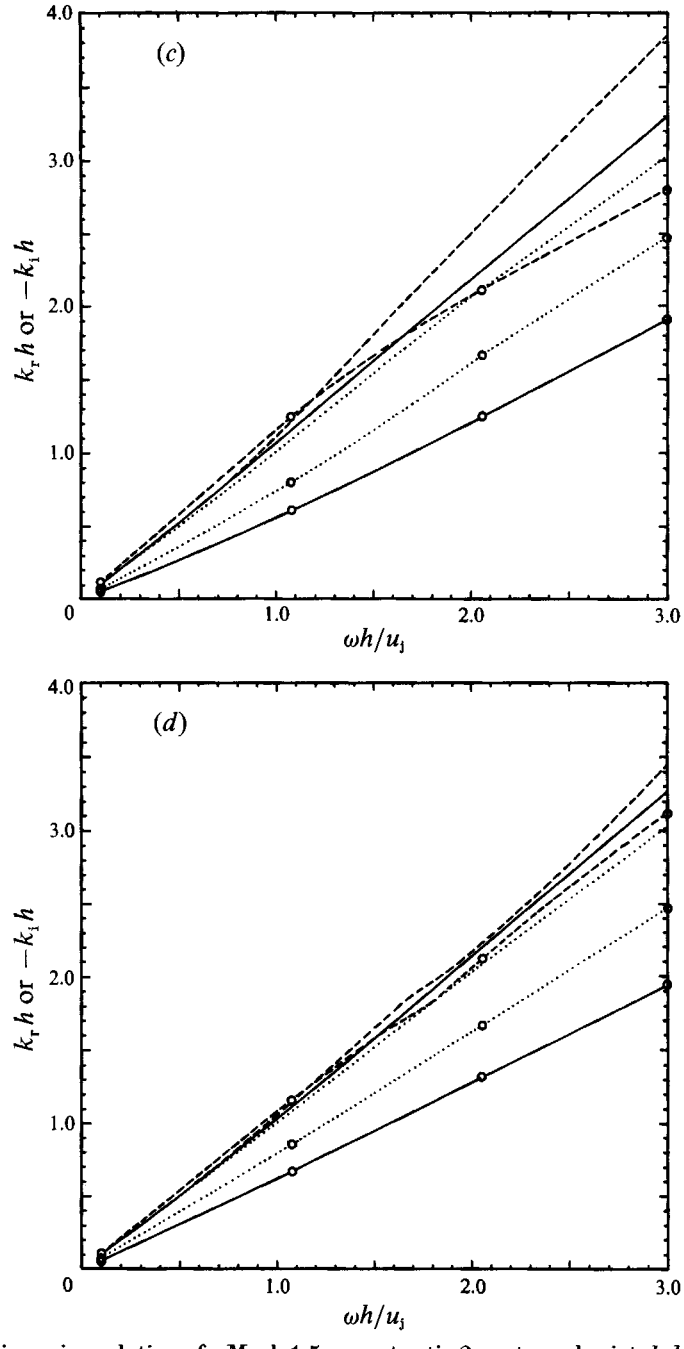

FIGURE 8. Dispersion relation of a Mach 1.5, aspect ratio 2, rectangular jet. $k_r h$ versus $\omega h/u_j$: ——, mode 1; – – –, mode 2; · · · · ·, mode 3. $-k_i h$ versus $\omega h/u_j$: ○——○, mode 1; ○– –○, mode 2; ○· ·○, mode 3. (*a*) Family 1, (*b*) family 2, (*c*) family 3, (*d*) family 4.

This is true even for jets with larger aspect ratios. Figure 9 (*a–d*) shows the dispersion relations for a similar jet but with an aspect ratio of four. As is evident, again the k_r versus ω relation for each wave mode can be closely approximated by a straight line. What this means is that the instability waves are non-dispersive. This non-

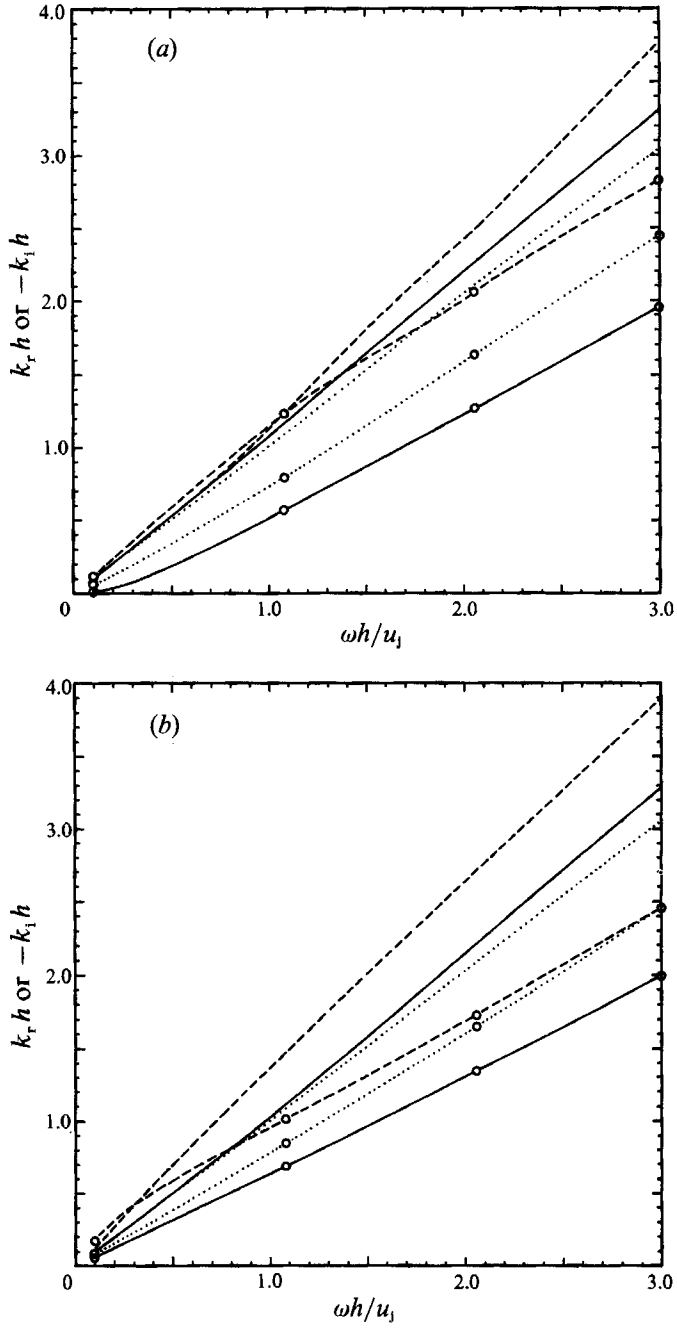

FIGURE 9(a, b). For caption see facing page.

dispersiveness characteristic of the instability waves of rectangular jets is not restricted to supersonic Mach numbers. Figure 10(a–d) shows the dispersion relations of a Mach 0.8, subsonic jet with aspect ratio four. The k_r versus ω curves are also quite linear. The present results indicate that regardless of Mach number and aspect ratio (the present computational study covers the range of Mach number up to 2.0 and aspect ratio up to 4) the instability waves of a rectangular jet with a thin

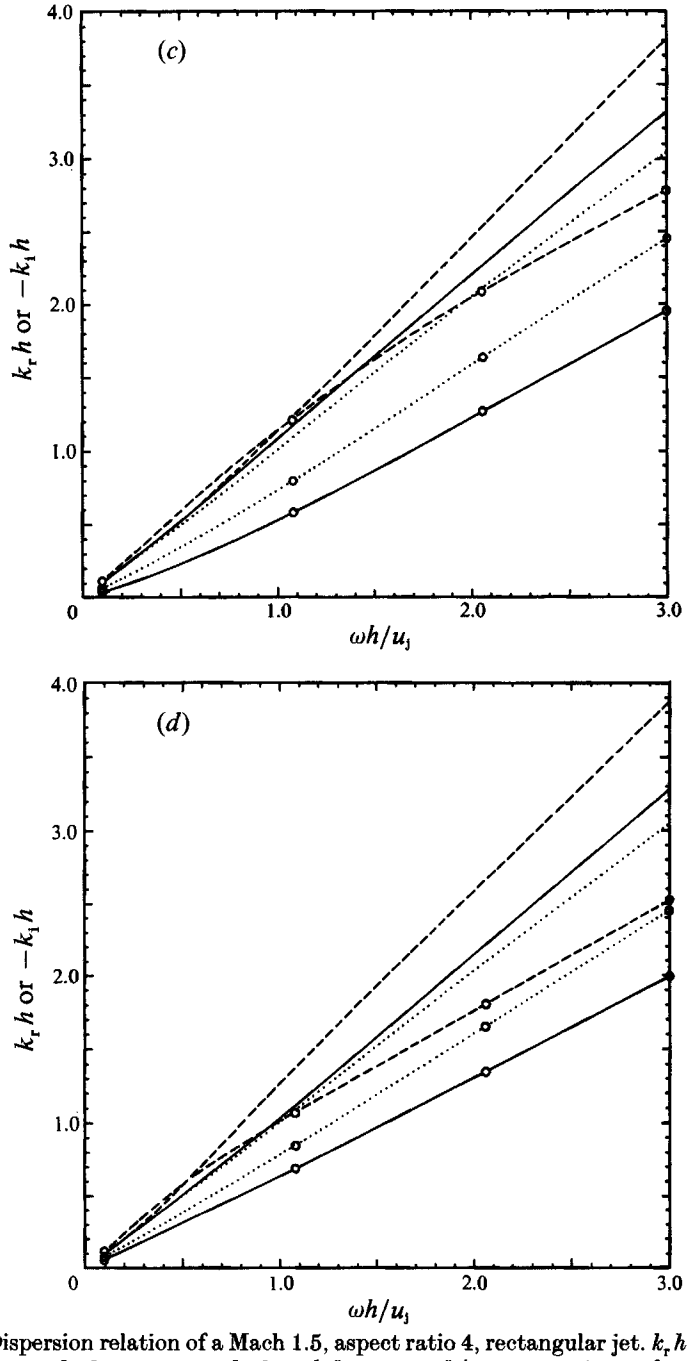

FIGURE 9. Dispersion relation of a Mach 1.5, aspect ratio 4, rectangular jet. $k_r h$ versus $\omega h/u_j$: ——, mode 1; – – –, mode 2; · · · · ·, mode 3. $-k_i h$ versus $\omega h/u_j$: ○——○, mode 1; ○– –○, mode 2; ○· ·○, mode 3. (*a*) Family 1, (*b*) family 2, (*c*) family 3, (*d*) family 4.

mixing layer are essentially non-dispersive. A closer examination of all the computed dispersion relations reveals that regardless of wave family, the first and third modes have phase velocities just slightly less than the jet speed. The second mode, however, has lower phase velocity (generally in the range of $0.8u_j$ to $0.9u_j$).

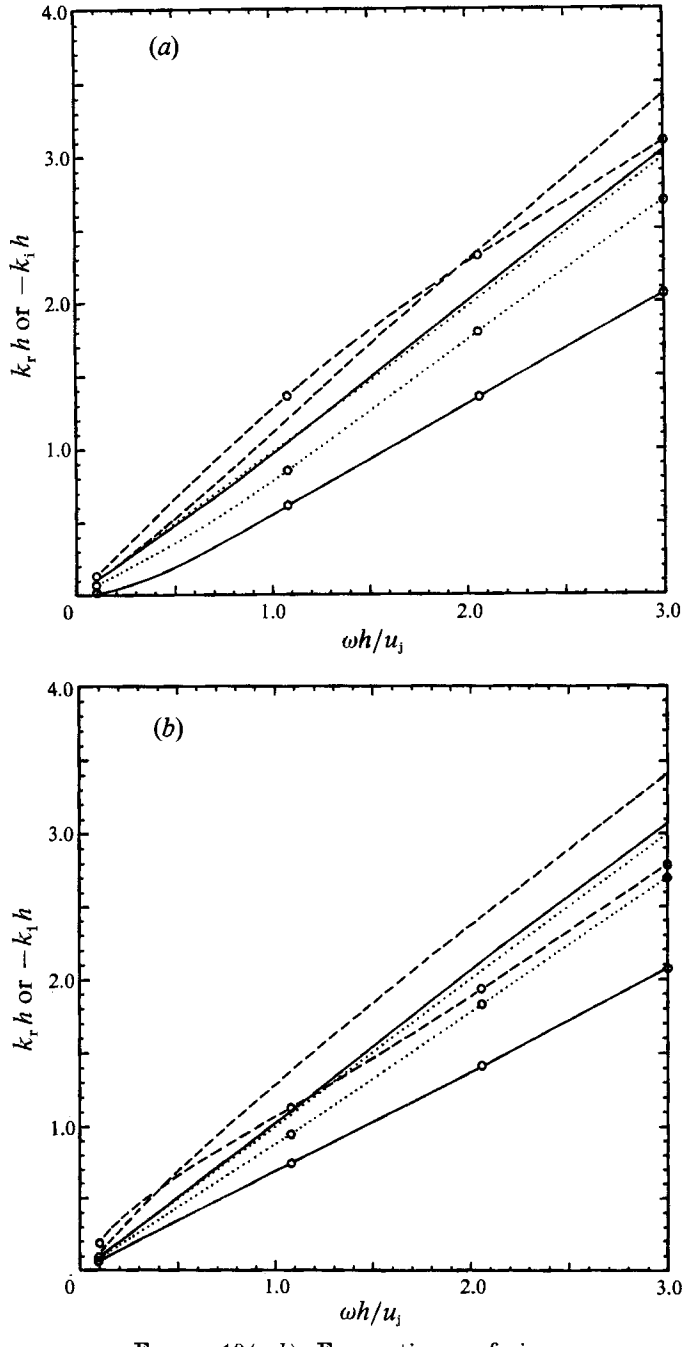

FIGURE 10(a, b). For caption see facing page.

Another interesting observation of the dispersion relations is that, independent of wave family and aspect ratio, the growth rates of the instability waves at a given jet Mach number, Strouhal number and mode number are comparable. This general statement can easily be verified by examining all the $-k_i$ versus ω relations of figures 8, 9 and 10. Furthermore, this same set of dispersion relations supports the rather unexpected conclusion that regardless of wave family, Mach number and aspect

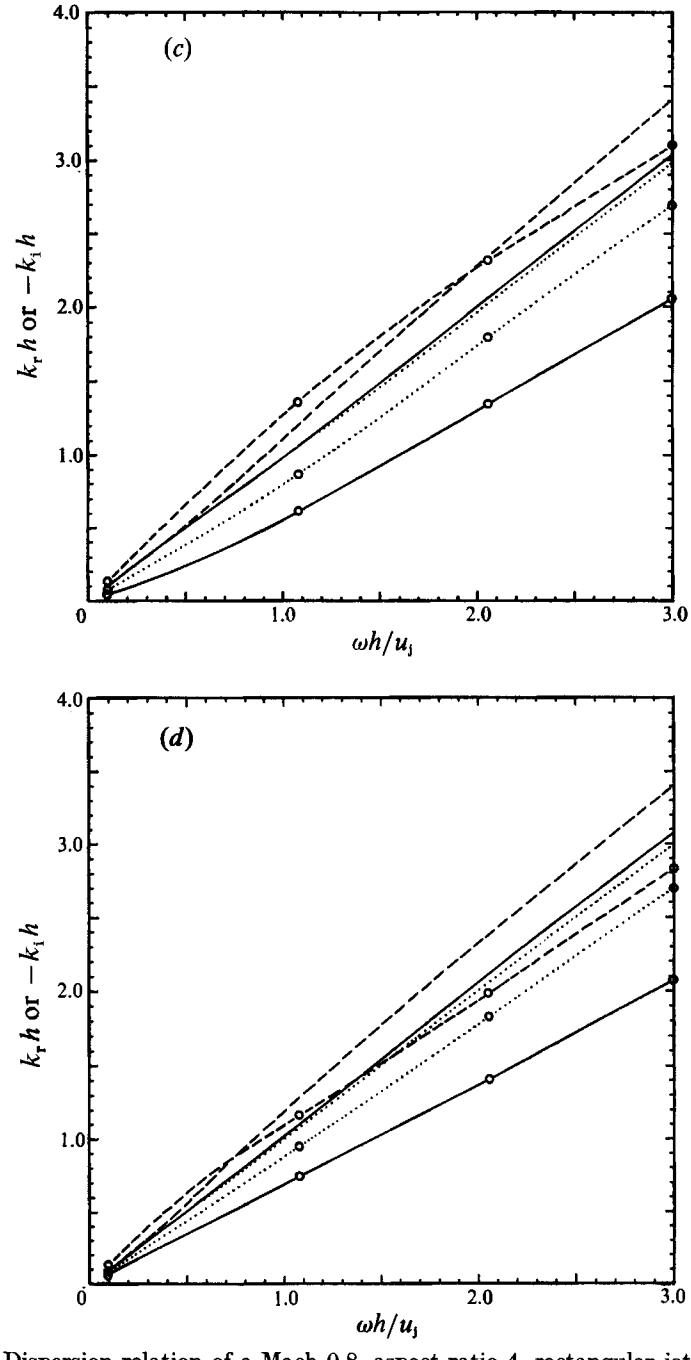

FIGURE 10. Dispersion relation of a Mach 0.8, aspect ratio 4, rectangular jet. $k_r h$ versus $\omega h/u_j$: ——, mode 1; – – –, mode 2; · · · · ·, mode 3. $-k_i h$ versus $\omega h/u_j$: O——O, mode 1; O– –O, mode 2; O · · O, mode 3. (*a*) Family 1, (*b*) family 2, (*c*) family 3, (*d*) family 4.

ratio, for a given Strouhal number, the second instability wave mode always has the highest spatial growth rate. This is a useful and important conclusion. It implies that the second mode could be the dominant mode. That is, this mode is most likely to be observed.

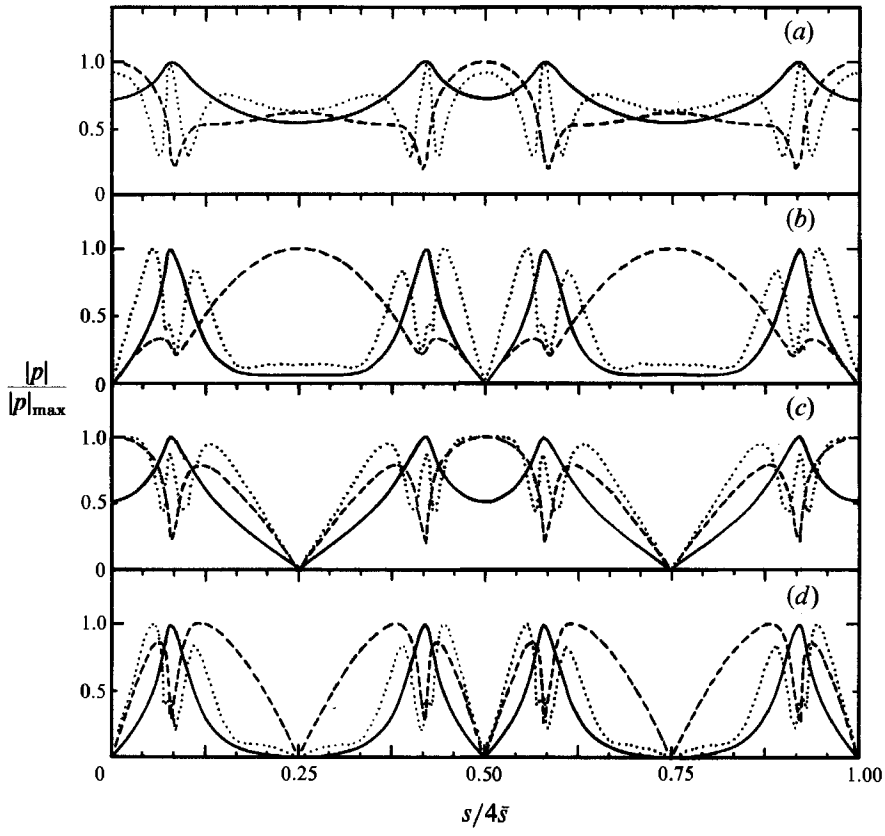

FIGURE 11. Distribution of $|p|$ along the thin shear layer of a Mach 1.5, aspect ratio 2, rectangular jet when $\omega h/u_j = 1.0$: ——, mode 1; – – –, mode 2; · · · · ·, mode 3. (*a*) Family 1, (*b*) family 2, (*c*) family 3, (*d*) family 4.

There appears no obvious explanation of why the second mode should always have the largest growth rate irrespective of the aspect ratio of the jet. To find a plausible explanation an examination of the (pressure) eigenfunction distributions has been carried out. Figure 11 shows the distribution of $|p|$ along the thin shear layer of a Mach 1.5, rectangular jet of aspect ratio 2 at a Strouhal number $\omega h/u_j = 1.0$. Notice that the corners of the jet are located at $s/(4\bar{s}) = 0.08, 0.42, 0.58, 0.92$. It can be seen that the maximum values of the pressure fluctuations of the mode 1 and mode 3 instability waves are concentrated near the four corners of the jet, whereas those of the second mode are largest near the middle or centre part of the jet. In this sense modes 1 and 3 are corner modes while mode 2 is a centre mode.

Figure 12 provides another illustration of the difference in eigenfunction distribution among the first three modes. The case considered is that of a Mach 1.5, supersonic jet with aspect ratio 4 and a Strouhal number $\omega h/u_j = 3.0$. It is easily seen that there is a distinct difference between the locations of the peaks in the spatial distribution of $|p|$ of mode 2 and the other two modes. Figure 13(*a–c*) provides contour maps of the spatial distributions of $|p|$ in the first quadrant for a Mach 1.5, aspect ratio 2 jet at $\omega h/u_j = 1.5$. Figures 13(*a*) and 13(*c*) show clearly that the pressure fluctuations associated with mode 1 and mode 3 (family 1) instability waves are highly localized near the corners of the jet. This is especially true for mode 1. Figure 13(*b*) indicates that the maximum pressure fluctuations of the mode 2

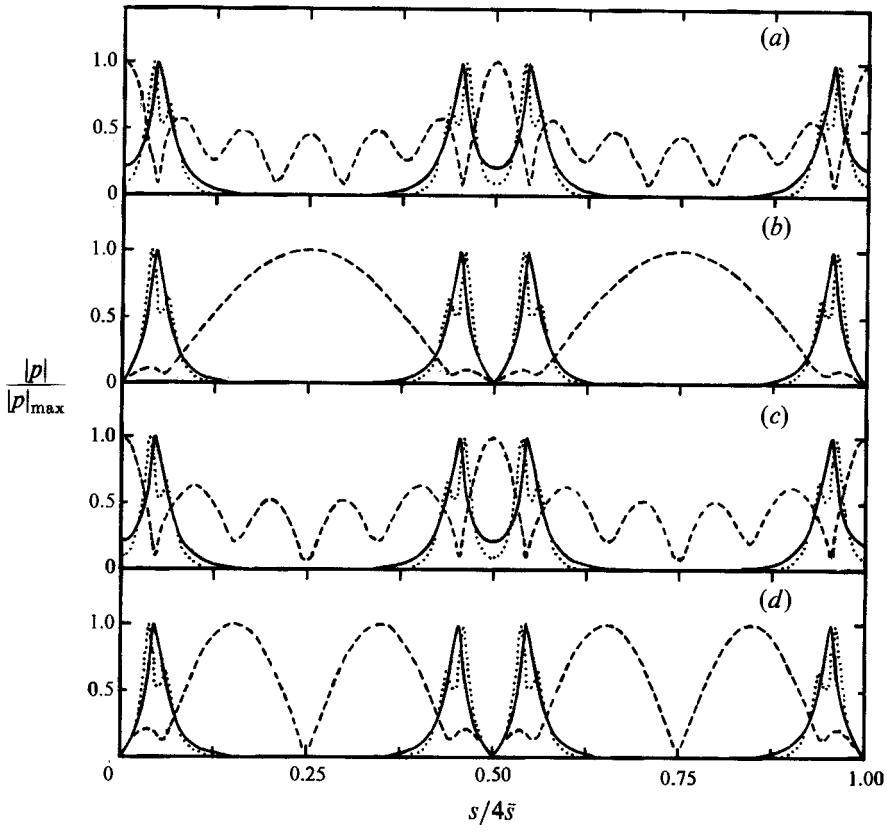

FIGURE 12. Distribution of $|p|$ along the thin shear layer of a Mach 1.5, aspect ratio 4, rectangular jet when $\omega h/u_j = 3.0$: ——, mode 1; – – –, mode 2; · · · · ·, mode 3. (*a*) Family 1, (*b*) family 2, (*c*) family 3, (*d*) family 4.

instability waves are concentrated near the shear layer in the middle of the jet. Now the fluctuations of the corner modes involve only a limited portion of the jet fluid mainly near the four corners of the jet. On the other hand, the centre mode (mode 2) involves a large part of the jet flow. Perhaps it is simply because of this that mode 2 always has a larger growth rate than the other two modes.

6. Discussion

In this study the instability of rectangular jets has been analysed using a vortex-sheet jet model. Because of this thin-shear-layer approximation, strictly speaking, the results are only applicable to the region of the jet immediately downstream of the nozzle exit. However, it appears, based on what has been found, that it is possible to infer qualitatively the different roles that the different instability wave modes play beyond the initial region of the jet.

It is known that flow instability is a key mechanism for promoting mixing in jets and other free shear flows. For rectangular jets the highly localized corner instability modes would quickly induce significant mixing and thus rounding off of the corners of the jets. In other words, these modes tend to assist the jet flow to evolve into a more circular cross-section in the downstream direction. Although an analysis of such jets with finite-thickness mixing layers is needed to provide a definitive

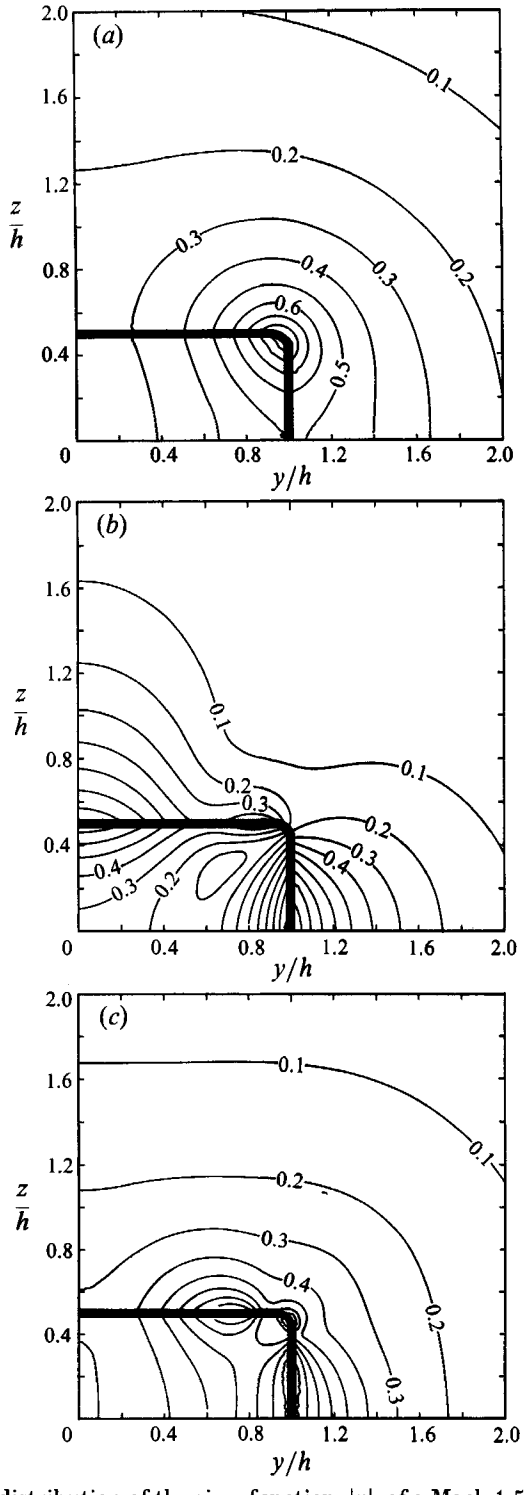

FIGURE 13. Spatial distribution of the eigenfunction, $|p|$, of a Mach 1.5, aspect ratio 2, rectangular jet (26 boundary elements) for family 1 with $\omega h/u_j = 1.5$. (*a*) mode 1, $kh = 1.6313–0.8395\mathrm{i}$; (*b*) mode 2, $kh = 1.7811–1.5427\mathrm{i}$; (*c*) mode 3, $kh = 1.5374–1.1586\mathrm{i}$.

statement, it is reasonable to expect that the corner modes would become damped downstream once the corners of the jet start disappearing. From this standpoint the corner modes are short-lived. The centre modes (mode 2), on the other hand, are supported by the entire jet flow. They would be able to persist downstream even when the jet becomes more circular in shape. Therefore, it is justifiable to assume that the centre modes would eventually develop into the dominant instability of the jet. If one's interest is in mixing and jet noise radiation, they would be the instability wave modes to study and measure.

This work was supported by NASA Langley Research Center Grant NAG 1-421.

Appendix. Integral with singular integrand

The only integral with a singular integrand among all the elements of determinant (4.4) is in μ_{ii}. Let the length of the boundary element be Δs and ξ be the distance measured from the centre of the element. It is easy to find

$$\mu_{ii} = \int_{-\Delta s/2}^{\Delta s/2} \tfrac{1}{4}\mathrm{i}H_0^{(1)}(\lambda|\xi|)\,\mathrm{d}\xi = \tfrac{1}{2}\mathrm{i}\int_0^{\Delta s/2} H_0^{(1)}(\lambda\eta)\,\mathrm{d}\eta.$$

Now change the variable of integration to ζ which is related to η by $\eta = \frac{1}{8}(\zeta+1)^2\Delta s$. This gives

$$\mu_{ii} = \frac{\mathrm{i}\Delta s}{8}\int_{-1}^{+1} H_0^{(1)}\left(\frac{\lambda\Delta s}{8}(\zeta+1)^2\right)(\zeta+1)\,\mathrm{d}\zeta$$

which has a regular integrand.

REFERENCES

Ahuja, K. K., Manes, J. P., Massey, K. C. & Calloway, A. B. 1990 An evaluation of various concepts of reducing supersonic jet noise. *AIAA Paper* 90-3982.

Baty, R. S. & Morris, P. J. 1989 Instability of jets of arbitrary geometry. *AIAA Paper* 89-1796.

Beskos, D. E. 1987 *Boundary Element Methods in Mechanics*. North-Holland.

Brebbia, C. A., Telles, J. C. F. & Wrobel, L. C. 1984 *Boundary Element Techniques*. Springer.

Bridges, T. J. & Morris, P. J. 1984 Differential eigenvalue problems in which the parameter appears nonlinearly. *J. Comput. Phys.* **55**, 437–460.

Crighton, D. G. 1973 Instability of an elliptic jet. *J. Fluid Mech.* **59**, 665–672.

Davidenko, D. F. 1960 The evaluation of determinants by the method of variation of parameters. *Sov. Math. Dokl.* **1**, 316–319.

Gaster, M., Kit, E. & Wygnanski, I. 1985 Large scale structures in a forced turbulent mixing layer. *J. Fluid Mech.* **150**, 23–39.

Gutmark, E., Schadow, K. C. & Bicker, C. J. 1990 Near acoustic field and shock structure of rectangular supersonic jets. *AIAA J.* **28**, 1163–1170.

Gutmark, E., Schadow, K. C., Wilson, K. J. & Bicker, C. J. 1988 Near-field pressure radiation and flow characteristics in low supersonic circular and elliptic jets. *Phys. Fluids* **31**, 2524–2532.

Koshigoe, S., Gutmark, E. & Schadow, K. C. 1988 Wave structure in jets of arbitrary shape. III. Triangular jets. *Phys. Fluids* **31**, 1410–1419.

Koshigoe, S. & Tubis, A. 1986 Wave structures in jets of arbitrary shape. I. Linear inviscid spatial instability analysis. *Phys. Fluids* **29**, 3982–3993.

Koshigoe, S. & Tubis, A. 1987 Wave structures in jets of arbitrary shape. II. Application of a generalized shooting method to linear instability analysis. *Phys. Fluids* **30**, 1715–1723.

Krothapalli, A., Hsia, Y., Baganoff, D. & Karamchetti, K. 1986 The role of screech tones in mixing of an underexpanded rectangular jet. *J. Sound Vib.* **106**, 119–143.

Morris, P. J. 1988 Instability of elliptical jets. *AIAA J.* **26**, 172–178.

PETERSEN, R. A. & SAMET, M. M. 1988 On the preferred mode of jet instability. *J. Fluid Mech.* **194**, 153–173.

PLASCHKO, P. 1981 Stochastic model theory for coherent turbulent structures in circular jets. *Phys. Fluids* **24**, 187–193.

PLASCHKO, P. 1983 Axial coherence functions of circular turbulent jets based on an inviscid calculation of damped modes. *Phys. Fluids* **26**, 2368–2372.

SCHADOW, K. S., GUTMARK, E., KOSHIGOE, S. & WILSON, K. J. 1989 Combustion-related shear-flow dynamics in elliptic supersonic jets. *AIAA J.* **27**, 1347–1353.

SEINER, J. M., PONTON, M. K. & MANNING, J. C. 1986 Acoustic properties associated with rectangular geometry supersonic nozzles. *AIAA Paper* 86-1867.

TAM, C. K. W. & BURTON, D. E. 1984 Sound generated by instability waves of supersonic flows. Part 2. Axisymmetric jets. *J. Fluid Mech.* **138**, 273–295.

TAM, C. K. W. & CHEN, K. C. 1979 A statistical model of turbulence in two-dimensional mixing layers. *J. Fluid Mech.* **92**, 303–326.

TAM, C. K. W. & HU, F. Q. 1989 On the three families of instability waves of high-speed jets. *J. Fluid Mech.* **201**, 447–483.

TAM, C. K. W. & MORRIS, P. J. 1985 Tone excited jets. Part V. A theoretical model and comparison with experiment. *J. Sound Vib.* **102**, 119–151.

WLEZIEN, R. W. & KIBENS, V. 1988 Influence of nozzle asymmetry on supersonic jets. *AIAA J.* **26**, 27–33.